JBC ARTICLE

Dimerization interface of osteoprotegerin revealed by hydrogen–deuterium exchange mass spectrometry

Received for publication, June 15, 2018, and in revised form, September 20, 2018 Published, Papers in Press, September 25, 2018, DOI 10.1074/jbc.RA118.004489

Yiming Xiao[‡1], Miaomiao Li[§1], Rinzhi Larocque[§], Fuming Zhang[¶], Anju Malhotra[¶], Jianle Chen[¶], Robert J. Linhardt[¶], Lars Konermann[‡2], and Ding Xu[§3]

From the [‡]Department of Chemistry, University of Western Ontario , London, Ontario N6A 5B7, Canada, the [§]Department of Oral Biology, University of Buffalo, Buffalo, New York 14214, and the [¶]Department of Chemical and Biological Engineering, Center for Biotechnology and Interdisciplinary Studies, Rensselaer Polytechnic Institute, Troy, New York 12180

Edited by Wolfgang Peti

Previous structural studies of osteoprotegerin (OPG), a crucial negative regulator of bone remodeling and osteoclastogenesis, were mostly limited to the N-terminal ligand-binding domains. It is now known that the three C-terminal domains of OPG also play essential roles in its function by mediating OPG dimerization, OPG–heparan sulfate (HS) interactions, and formation of the OPG–HS–receptor activator of nuclear factor κB ligand (RANKL) ternary complex. Employing hydrogen–deuterium exchange MS methods, here we investigated the structure of full-length OPG in complex with HS or RANKL in solution. Our data revealed two noteworthy aspects of the OPG structure. First, we found that the interconnection between the N- and C-terminal domains is much more rigid than previously thought, possibly because of hydrophobic interactions between the fourth cysteine-rich domain and the first death domain. Second, we observed that two hydrophobic clusters located in two separate C-terminal domains directly contribute to OPG dimerization, likely by forming a hydrophobic dimerization interface. Aided by site-directed mutagenesis, we further demonstrated that an intact dimerization interface is essential for the biological activity of OPG. Our study represents an important step toward deciphering the structure–function relationship of the full-length OPG protein.

Osteoprotegerin (OPG)[4] plays a crucial role in bone remodeling by acting as a decoy receptor that inhibits the activity of RANKL (receptor activator of nuclear factor κ-B ligand), an essential osteoclastogenic factor (1, 2). OPG belongs to the tumor necrosis factor receptor superfamily but is expressed as a secreted soluble protein. OPG is a highly flexible multidomain protein that can be dissected into seven domains (Fig. 1*A*) (3, 4). The N-terminal half of OPG contains four cysteine-rich domains (CRD1–CRD4), which harbor numerous intramolecular disulfide bonds. The second half of the sequence contains two death domains (DD1 and DD2) and a short C-terminal domain (tail domain hereafter). Previous studies have shown that CRD2 and CRD3 are responsible for RANKL binding, whereas DD2 and the tail domain mediate binding to heparan sulfate (HS) (3–5). The biological function of DD1 remains unknown.

OPG exists naturally in monomeric and dimeric states (1, 6). Exactly why both forms are produced, and whether there is any difference in the biological function of the two forms, remains unknown. The main dimerization mechanism has been believed to be the formation of an intermolecular disulfide bond at the penultimate Cys-400 (4, 5). We will refer to this SS-linked homodimer as OPG_2^{SS}, as opposed to monomeric OPG^{SH}, which lacks the covalent linkage (the "SH" superscript indicates the free sulfhydryl groups of Cys-400). However, recent work in our laboratory has revealed a previously unknown mechanism of OPG dimerization, which involves binding to HS (5). Interestingly, formation of the HS-dependent OPG dimer (referred to as $[OPG^{SH}]_2$) does not require the intermolecular disulfide, as the C400A mutant of OPG also undergoes HS-induced dimerization (5). This finding makes it highly likely that there is an unidentified dimerization interface.

X-ray crystallography has provided some insights into the interaction of OPG with RANKL (3, 7). Fig. 1, *B* and *C*, depict the structure of a 3:3 complex between the RANKL receptor-binding domain (*gray*) and the CRD1–CRD4 domains of OPG (*colored*). RANKL is a trimer and each of its subunits interacts with one OPG chain. These interactions are mediated by segments ^{71}TDSWHTSDECVYCSPVCKEL^{90} and ^{111}RYLEIEFC^{118} in CRD2 and CRD3, respectively (3). Fig. 1*C* displays the remaining OPG regions (DD1, DD2, Tail) in diagram form due to the lack of crystallographic information for these segments. Given the propensity of OPG to dimerize (1, 4),

This work was supported by National Institutes of Health NIAMS Grant AR070179, NIDDK Grant DK111958, and NHLBI Grants HL125371 and HL094463 and Canadian Network for Research and Innovation in Machining Technology, Natural Sciences and Engineering Research Council of Canada (CANRIMT, NSERC) Grant RGPIN-2018–04243. The authors declare that they have no conflicts of interest with the contents of this article. The content is solely the responsibility of the authors and does not necessarily represent the official views of the National Institutes of Health.

This article contains Table S1 and Figs. S1–S6.

[1] Both authors contributed equally to the results of this work.

[2] To whom correspondence may be addressed. Tel.: 519-661-2111 (ext. 86313); E-mail: konerman@uwo.ca.

[3] To whom correspondence may be addressed: Tel.: 716-829-3509; E-mail: dingxu@buffalo.edu.

[4] The abbreviations used are: OPG, osteoprotegerin; RANKL, receptor activator of nuclear factor κB ligand; HS, heparan sulfate; RANK, receptor activator of nuclear factor κB; CRD, cysteine-rich domains; DD, death domain; HDX, hydrogen–deuterium exchange; SEC, size exclusion chromatography; WT, wildtype; TRAP, tartrate-resistant acid phosphatase; SPR, surface plasmon resonance; APLP-1, amyloid precursor-like protein 1; RAGE, receptor for advance glycation end product; mOPG, mouse OPG; PDB, Protein Data Bank; TCEP, tris(2-carboxyethyl)phosphine.

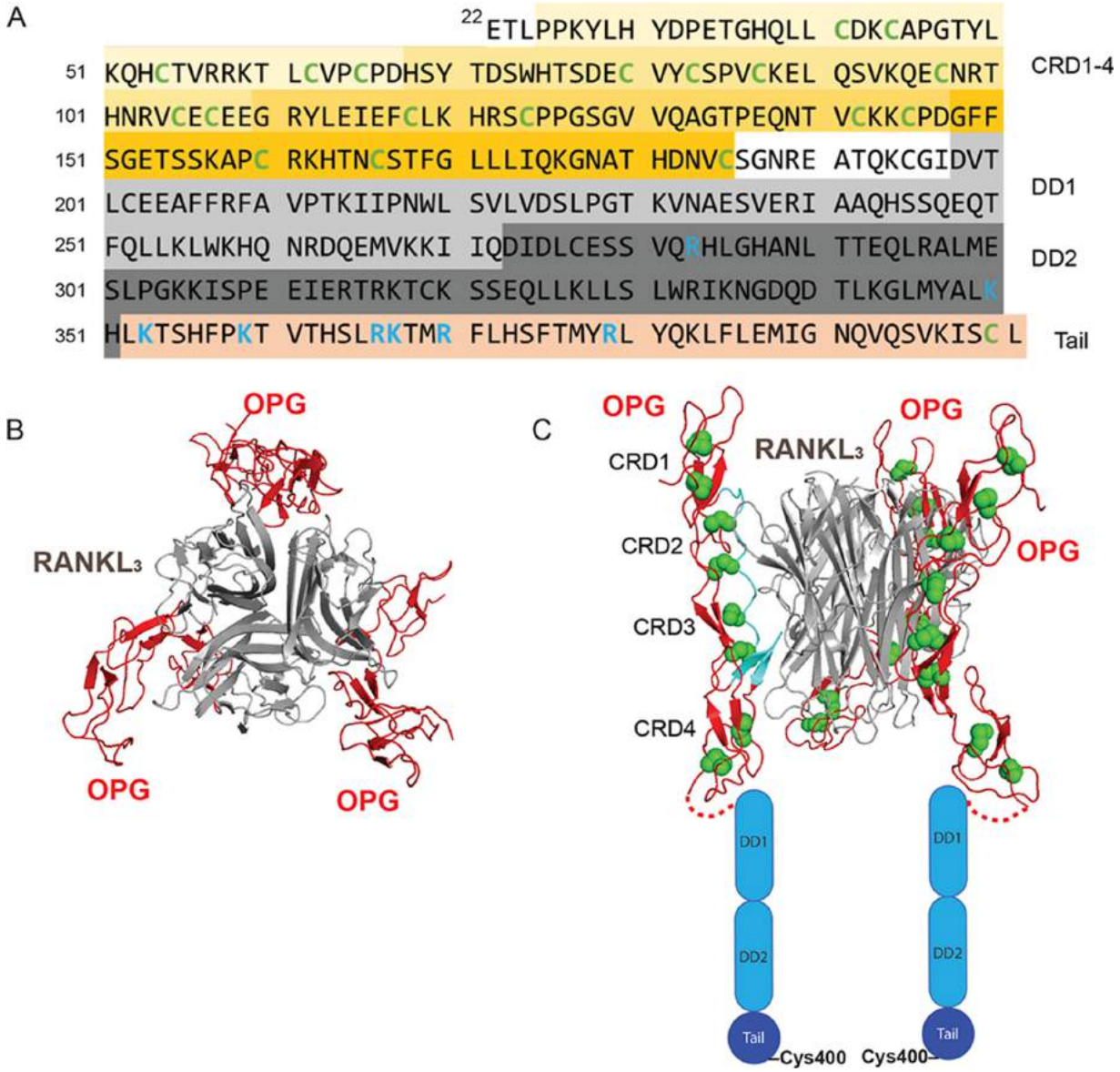

Figure 1. OPG sequence and domain structure. *A,* mouse OPG sequence and domain structure. Cysteine residues involved in disulfide bonds are shown in *green*. Basic residues that are responsive for HS binding are shown in *blue*. *B,* crystal structure of a complex consisting of three truncated OPG monomers and trimeric truncated RANKL (PDB code 4E4D). View from the OPG N-terminal side. *C,* side view of the same structure, with key contact regions highlighted in *cyan* for one of the OPG chains. Disulfides are shown in *green spheres*. Representations of the two OPG death domains (DD1 and DD2) and the tail domain containing Cys-400 involved intermolecular disulfide interactions are shown.

the main physiological binding scenario likely involves two subunits of the RANKL trimer that interact with one OPG dimer (7). The third RANKL subunit can bind a second OPG dimer, but likely with lower affinity because that interaction would only involve a single RANKL chain and a single OPG chain (8). Of note, our laboratory has recently reported that RANKL, OPG, and HS can form a stable ternary complex. Based on size exclusion chromatography (SEC), the stoichiometry of the complex is consistent with a RANKL trimer interacting with two OPG dimers (5).

Despite these insights, our knowledge unfortunately only extends to truncated constructs because full-length OPG has not been amenable to crystallographic investigations. As a result, the structure of the three C-terminal domains, the spatial relationship between the CRDs and the C-terminal domains, and the structural details of OPG dimerization remain unknown. In addition, gaining structural insights of the C-terminal domains is especially important for deciphering how HS binding to the C-terminal domains regulates formation of the newly discovered HS–OPG–RANKL ternary complex (5). Filling this significant knowledge gap would require another experimental method to probe the structure and dynamics of full-length OPG in solution. Hydrogen–deuterium exchange (HDX) has emerged as a powerful tech-

nique to probe the structure and dynamics of proteins in solution (9). Founded on the basis that backbone NH hydrogen atoms are labile and can exchange with deuterium from the solvent, HDX-MS is well-suited to probe structural changes experienced by proteins during intermolecular interactions. We and others have shown that HDX-MS can provide detailed information on ligand–protein and protein–protein contacts (9–15). Such interactions usually stabilize the protein in the vicinity of the binding site, thereby reducing the extent of H-bond opening/closing fluctuations such that the corresponding regions become more protected. Although H-bond fluctuations are believed to be the main determinant of HDX rates (16), other factors such as the electrostatic environment of NH sites may also play a certain role (17, 18).

Guided by comprehensive HDX-MS analysis of purified OPG^{SH} and OPG_2^{SS} in complex with HS and/or RANKL, here we report the identification of two hydrophobic regions, located in DD1 and in the tail domain, which are required for forming OPG_2^{SS}. We further show that these hydrophobic residues are also involved in forming a HS-induced dimer $[OPG^{SH}]_2$. We also provide evidence that the newly discovered hydrophobic dimerization interface works synergistically with HS to stabilize the dimer, which we found is required for the optimal inhibitory potency of OPG toward RANKL. Additionally, our HDX data reveal that the interconnection between the N-terminal and C-terminal domains is likely much more intimate than previously predicted, which might represent an important link to understand the interplay between the ligand-binding N-terminal and C-terminal domains.

Results

OPG^{SH} binds HS with significantly lower affinity than OPG_2^{SS}

We and others have previously shown that monomeric OPG^{SH} was eluted from heparin-Sepharose at much lower salt concentrations compared with OPG_2^{SS} (750 *versus* 1050 mM) (4, 5). Here, by using surface plasmon resonance (SPR), we determined that the binding affinity of OPG^{SH} to immobilized HS is 17-fold weaker than that of OPG_2^{SS} (290 *versus* 17 nM, Fig. 2, *A* and *B*, and Table 1). Kinetic analyses of the SPR sensorgrams suggest that the main factor contributing to the weaker HS binding of OPG^{SH} is the dramatically reduced association rate (30-fold, from 8.9×10^5 to 3×10^4 M s^{-1}). Consistent with these SPR data, the apparent binding affinity of OPG^{SH} to osteoblast cell-surface HS was only 60 nM, (Fig. 2*C*), which represents a 50-fold reduction in affinity compared with OPG_2^{SS} (5).

OPG^{SH} is naturally made in the bone marrow

Although secretion of OPG^{SH} has been documented in cell culture systems (6), it remains unknown whether OPG^{SH} truly exists in living animals, or if it immediately gets converted to OPG_2^{SS}. To test this, we examined the OPG^{SH}/OPG_2^{SS} ratio in murine bone marrow plasma. Based on the much lower binding affinity of OPG^{SH} to cell-surface HS (Fig. 2*C*), we devised a method to quantify OPG^{SH} and OPG_2^{SS}. The whole bone marrow content was first resuspended with a small volume of PBS to recover the unimmobilized portion of OPG. Next, the cell pellet was washed quickly with 1.5 M NaCl to elute the OPG that was immobilized by binding to cell-surface HS. Both portions were then analyzed by heparin-Sepharose chromatography and the eluted fractions were analyzed by ELISA to quantify the amount of OPG. We found that the soluble portion of OPG eluted from the heparin-Sepharose as a very broad peak at salt

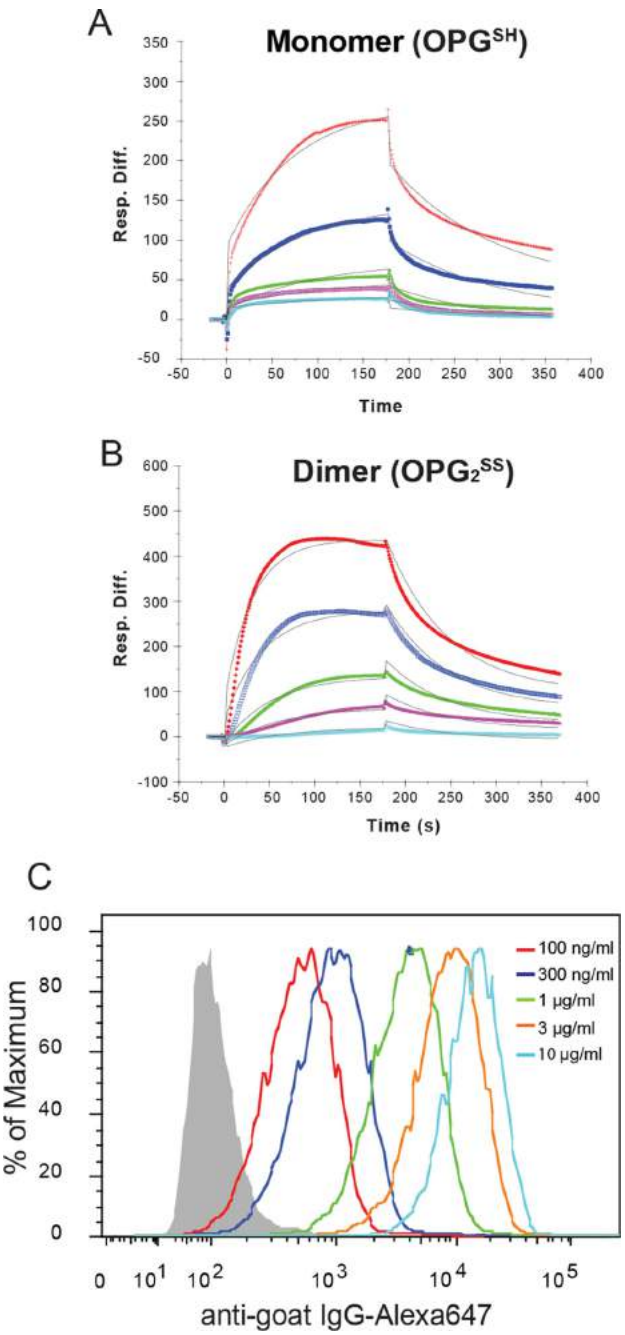

Figure 2. Binding of OPG monomer (OPG^{SH}) and dimer (OPG_2^{SS})to HS. *A,* SPR sensorgrams of OPG-HS interaction. Concentrations of monomer (from top to bottom): 160, 80, 40, 20, and 10 nM, respectively. *B,* concentrations of dimer (from top to bottom): 20, 10, 5, 2.5, and 1.25 nM, respectively. The *black curves* are the fitting curves using models from BIAevaluate 4.0.1. *C,* binding of OPG monomer to MC3T3 cells was determined by a FACS-based binding assay. The bound mOPG were detected by staining with a goat anti-mOPG antibody, followed by anti-goat IgG-Alexa 647. The *shaded histogram* is from cells stained with only antibodies.

Table 1
Summary of kinetic data of OPG-HS interactions
Numbers in parentheses are the standard deviations (S.D.) from global fitting of five injections.

Protein	k_a	k_d	K_d
	$M^{-1}s^{-1}$	s^{-1}	M
OPG monomer	3.0×10^4 ($\pm 2.2 \times 10^3$)	8.7×10^{-3} ($\pm 2.2 \times 10^{-4}$)	2.9×10^{-7}
OPG dimer	8.9×10^5 ($\pm 3.2 \times 10^4$)	15×10^{-3} ($\pm 3.8 \times 10^{-4}$)	1.7×10^{-8}

concentrations between 550 and 1350 mM. This elution pattern precisely mirrors that of recombinant OPG, where OPG^{SH} eluted between 550 and 900 mM (fraction F6–F9), and OPG_2^{SS} between 900 and 1350 mM (fraction F9–F13, Fig. 3*A*). Interestingly, the soluble OPG contains roughly equal amounts of OPG^{SH} and OPG_2^{SS} (Fig. 3*B*), whereas the cell-surface bound portion contains 2.5-fold more OPG_2^{SS} than OPG^{SH} (Fig. 3*C*). The total fraction of OPG^{SH} present in the bone marrow is 45 ± 3% (average of two separate mouse samples). To our knowledge, our experiment is the first to show that monomeric OPG^{SH} is found naturally in mice.

Overall HDX pattern of OPG

HDX-MS was employed to interrogate changes in the structure and dynamics of full-length OPG^{SH} and OPG_2^{SS} in response to HS and/or RANKL addition. Eight conditions were tested: 1) OPG^{SH} alone, 2) OPG^{SH} + HS, 3) OPG^{SH} + HS + RANKL, 4) OPG^{SH} + RANKL, 5) OPG_2^{SS} alone, 6) OPG_2^{SS} + HS, 7) OPG_2^{SS} + HS + RANKL, and 8) OPG_2^{SS} + RANKL. In all samples we identified >60 peptides, for a sequence coverage of ~80%. The digestion patterns of OPG_2^{SS} and OPG^{SH} were slightly different. The large number of intramolecular disulfides in CRD1–CRD4 necessitated the implementation of a carefully optimized digestion protocol, because SS bonds are known to interfere with peptic digestion (19–22) (see "Experimental procedures" for details). However, even with this optimized protocol the number of peptides originating from CRD1–CRD4 was significantly lower than in the DD1/DD2/Tail regions (Figs. S1 and S2). The complete set of HDX kinetics recorded under all eight conditions is summarized in Figs. S3 and S4, and typical unprocessed mass spectra are exemplified in Fig. S5. Overall, a striking feature of the entire HDX-MS data set are the relatively high exchange levels for the vast majority of the peptides. Typical globular proteins tend to possess rigid segments that remain incompletely deuterated even after hours of D_2O incubation (10–15). OPG showed a very different behavior, as many peptides were ~50% labeled already after 10 s. After 100 min, deuteration had gone to completion for nearly all peptides, even in the presence of ligands. This behavior reflects the highly dynamic nature of OPG, which has thus far precluded crystallization of the full-length protein (3, 7). Difficulties of growing crystals from proteins that show high HDX levels have been noted previously (23).

Representative examples taken from the complete HDX data set (Figs. S3 and S4) are highlighted in Figs. 4 and 5, illustrating the behavior of various regions in OPG^{SH} (*left-hand side*) and OPG_2^{SS} (*right-hand side*). As noted above, the peptic cleavage patterns were somewhat different for the two forms. In Figs. 3 and 4 an effort was made to compare OPG^{SH} and OPG_2^{SS} peptides that cover approximately the same regions. The data interpretation is guided by the tenet that noncovalent intermolecular interactions often (though not always) cause reduced HDX levels. These HDX changes tend to be most pronounced directly at the interaction site, but allosteric effects may take place as well (24–27).

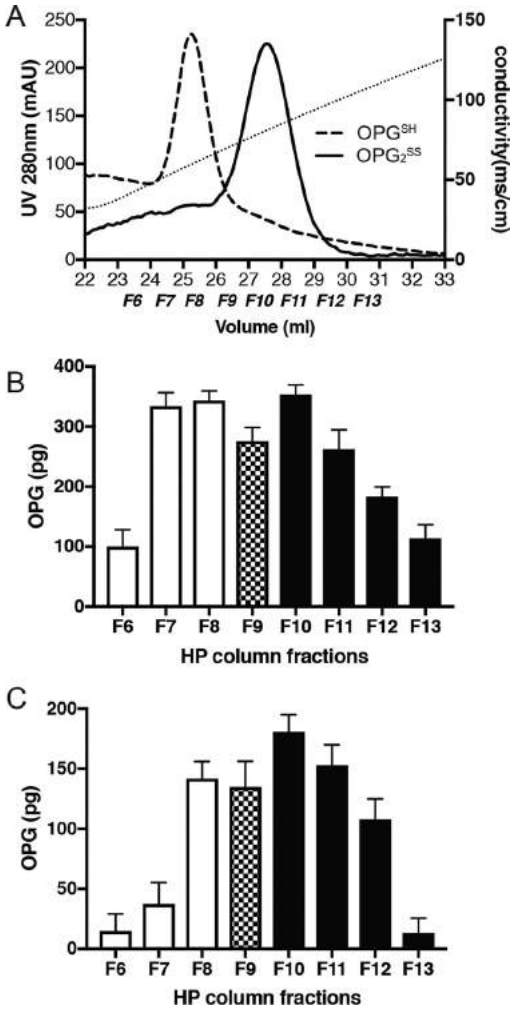

Figure 3. OPG^{SH} represents a significant portion of OPG generated in the bone marrow cavity. *A,* typical elution pattern of purified recombinant OPG^{SH} and OPG_2^{SS} on heparin-Sepharose column. The positions of the fractions F6–F13 are labeled under the *x*-axis. *B,* the PBS-wash fraction of bone marrow was run on a heparin column and the amount of OPG in each fractions was plotted. OPG in fractions F6–F8 was counted as OPG^{SH}, in fractions F10–F13 OPG was counted as OPG_2^{SS}, whereas F9 was counted as half OPG^{SH} and half OPG_2^{SS}. *C,* the high salt-wash fraction of bone marrow was run on a heparin column and the amount of OPG in each fractions was plotted.

HDX pattern in the CRDs

CRD1 (Fig. 4, *peptide 22–40*) was found to be quite dynamic, with high deuteration levels that were insensitive to addition of HS and/or RANKL. This behavior is consistent with the view that CRD1 is not involved in HS or RANKL binding, both in the case of OPG^{SH} and OPG_2^{SS} (3, 5, 7). CRD2 in OPG^{SH} appeared to be highly dynamic, regardless of the presence of HS or

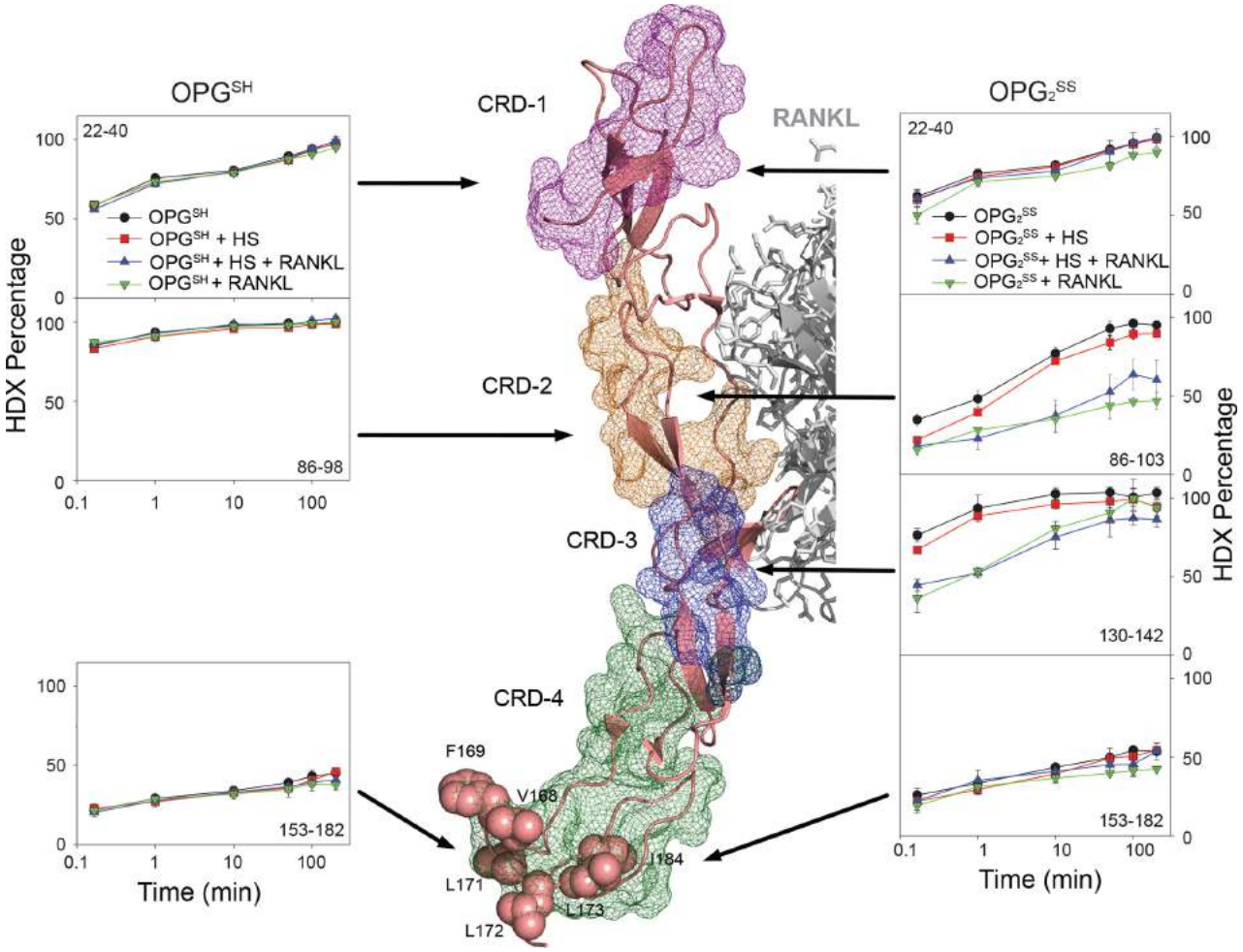

Figure 4. HDX kinetics of peptides that covers the RANKL-binding site. Individual peptides of OPG were highlighted with *mesh* representation. Bound RANKL is shown in *gray cartoon*. Residues located in the hydrophobic patch at the tip of CRD-4 domain are shown in space-filling representation. Structure is based on PDB code 3URF. Of note, kinetics graphs highlighted here are part of the full set shown in supporting Figs. S3 and S4.

RANKL (Fig. 4, *86–98*). In OPG_2^{SS} this segment was much more protected even without ligands (Fig. 4, *peptide 86–103*). This behavior strongly suggests the occurrence of noncovalent CRD2–CRD2′ binding interactions in OPG_2^{SS}, likely promoted by the "pre-alignment" of the two OPG chains by the C-terminal disulfide. Significant additional stabilization of CRD2 in OPG_2^{SS} was observed after addition of RANKL, and very similar effects were seen for CRD3 (Fig. 4, *130–142*). These findings are consistent with crystallographic data that identified CRD2 and CRD3 as RANKL-binding regions (3, 7). In contrast to peptide 86–103 of OPG_2^{SS}, which was greatly protected after RANKL binding, peptide 86–98 in OPG^{SH} did not display any protection from HDX. Of note, Luan *et al.* (7) have reported that mutating Asp-57 and Glu-58 in CRD2 (corresponds to Asp-78 and Glu-79 in our numbering) had no effect on OPG-RANKL interaction, which suggests that CRD2-RANKL contacts is in fact dispensable for OPG-RANKL interaction. Importantly, the OPG fragment (CRD1–CRD4) they used in the study was also monomeric. Therefore, their mutagenesis study and our HDX data together suggest that CRD2-RANKL contacts are dispensable for monomeric OPG-RANKL interaction. The fact that we did observe significant protection of CRD2 (peptide 86–103) of dimeric OPG_2^{SS} after RANKL binding suggests that whether CRD2 make contributions to RANKL binding in solution likely depends on the oligomeric states of OPG.

The only peptides in our dataset that did not display 100% deuteration at the end the HDX labeling period were located in (or close to) CRD4 (Fig. 4, 153–182; Fig. 5, 166–202). This stretch covers most of CRD4, the linker region, and the beginning portion of DD1. This finding suggests that CRD4 has the most stable secondary structure among all domains in OPG; this behavior is somewhat surprising because like all CRDs, CRD4 mostly consists of loops that lack extensive H-bonding in the crystal structure (7). The low HDX rate of CRD4 is independent of the dimerization status and RANKL or HS binding, suggesting that CRD4 interacts intramolecularly with other elements of OPG. In our view, the most likely scenario is that CRD4 interacts with the linker region (186–197), and the N-terminal tip of DD1. Interestingly, a high density of bulky hydrophobic residues (Phe-169, Leu-171, Leu-172, Leu-173, Ile-174, Val-184) are located at the C-terminal tip of the CRD4,

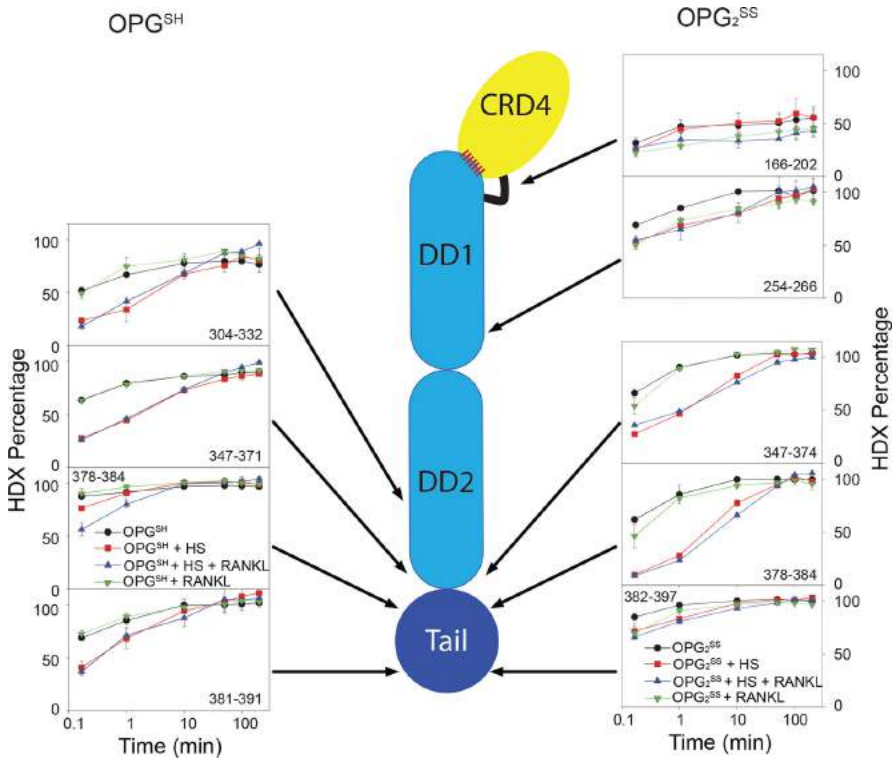

Figure 5. HDX kinetics of peptides that covers the C-terminal domains. A schematic diagram of the C-terminal domains of OPG is shown. The arrangement of CRD4, linker, and DD1 is based on the potential interdomain hydrophobic interactions (represented in *red sticks*). Of note, kinetics graphs highlighted here are part of the full set shown in supporting Figs. S3 and S4.

and the location of this hydrophobic cluster is depicted in Fig. 4 (Val-168, Phe-169, Leu-171, Leu-172, Leu-173, Ile-184 in human OPG). It is possible that this hydrophobic cluster forms intramolecular interactions with six highly conserved hydrophobic resides located at the N-terminal tip of DD1 (Ile-197, Val-199, Leu-201, Phe-206, Phe-207, Phe-209). In addition, two conserved cysteines (Cys-195 and Cys-202) are found in the linker region and the N-terminal tip of DD1, respectively, which could further increase the structural rigidity of the region via disulfide formation. Consistent with this proposal, peptides 199–206 and 191–220 of OPG^{SH} (Fig. S1) had significantly lower HDX levels in the first minute compared with all other peptides in DD1, suggesting the N-terminal portion of DD1 is relatively rigid.

HDX pattern in C-terminal domains

Like the CRD domains, the vast majority of DD1 and DD2 were highly dynamic in both OPG^{SH} and OPG_2^{SS}. Close inspection of the HDX profiles in these regions reveals many interesting features. In OPG_2^{SS}, two peptides stand out in that they showed significantly lower deuteration in the presence of HS (Fig. 5, 347–374 and 378–384). A similar effect of HS-binding on these peptides was also observed in OPG^{SH}. Remarkably, these peptides include 7 of 8 HS-binding residues that we previously identified by site-directed mutagenesis (Lys-350, Lys-353, Lys-359, Arg-366, Lys-367, Arg-370, and Arg-379) (5), which was a nice confirmation of the sensitivity and accuracy of HDX-MS in probing the structure of OPG.

Aside from the peptides that directly cover the HS-binding regions, we identified several additional regions that were protected from HDX in the presence of HS (Fig. 5, 381–391 and 304–332 in OPG^{SH}, 254–266 and 382–397 in OPG_2^{SS}). What is unique about these peptides is that they do not contain any HS-binding residues but instead harbor many conserved hydrophobic residues. The reason that these peptides became protected in HS–OPG dimeric complexes could be that they are part of the dimerization interface. In principle, because the dimerization interface becomes more stable in the presence of HS, the residues involved in dimerization should become more protected from HDX. Interestingly, these peptides are located in three regions that are far apart, with two peptides (381–391 in OPG^{SH} and 382–397 in OPG_2^{SS}) in the tail domain, one in the DD2 (304–332 in OPG^{SH}) and one in the DD1 (254–266 in OPG_2^{SS}). The HDX protection in DD2 and in the tail domain attributed to the combination of HS-protein interactions and HS-mediated protein-protein contacts is further highlighted in the difference plots of Fig. S6.

Identification of hydrophobic residues involved in forming OPG_2^{SS}

Because of the prominent role hydrophobic interactions play in protein oligomerization (28), we focused on the hydrophobic residues within the three aforementioned regions (254–266, 304–332, and 381–397). To narrow down the number of hydrophobic residues for mutagenesis, two criteria were used. First, we generated a death domain homology model using

Table 2
Dimer and monomer ratio of hydrophobic mutants as measured by heparin-Sepharose chromatography

Mutant name	Percentage in total yield	
	OPG^{SH} monomer	OPG_2^{SS} dimer
L254A	100%	0%
L256A	40%	60%
W257A	100%	0%
L326A	35%	66%
L331A	40%	60%
L380A	60%	40%
L384A	80%	20%
F385A	100%	0%
L386A	100%	0%
M388A	75%	25%
L389A	65%	35%
WT	40%	60%

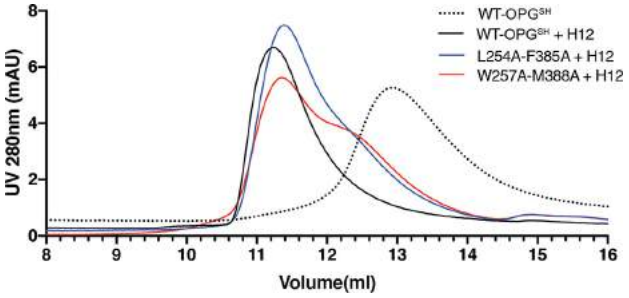

Figure 6. L254A,F385A and W257A,M388A OPG^{SH} show reduced HS-mediated dimerization. 30 μg (0.5 nmol) of mOPG OPG^{SH} was incubated with 1.8 μg (0.5 nmol) of HP-derived dodecasaccharide (H12) at room temperature for 2 h and resolved on a SEC column (Enrich650, Bio-Rad).

Phyre2 and used it to rule out those hydrophobic resides that are directly involved in protein folding (29). Second, those residues that are not conserved from human to *Xenopus* were excluded. Application of these two criteria prompted us to mutate 11 hydrophobic resides to alanine, and to examine their effects on OPG dimerization. When these mutants were tested by heparin-Sepharose chromatography, we found that 8 of the 11 mutations had significant reductions in OPG_2^{SS}, and 4 mutants (L254A, W257A, F385A, and L386A) were expressed exclusively as monomer (Table 2). Interestingly, none of the two mutants within the 304–332 peptide had any effect on the monomer/dimer ratio, whereas two out three mutants in DD1 and all mutants in the tail domain altered the monomer/dimer ratio. This result strongly suggests that the hydrophobic residues within the DD1 and the tail domain contribute to protein–protein contacts in OPG_2^{SS}.

Hydrophobic mutants show reduced HS-induced dimerization

To investigate whether the hydrophobic residues identified above (L254A, W257A, L380A, L384A, F385A, L386A, M388A and L389A) are also involved in HS-induced OPG dimerization, we incubated the monomeric hydrophobic mutants with heparin-derived dodecasaccharide (H12) and examined their ability to form $[OPG^{SH}]_2$ by SEC. To our surprise, none of the mutants displayed defects in H12-induced $[OPG^{SH}]_2$ dimerization (data not shown). We reasoned that it is likely that a single mutation in the hydrophobic interface is not severe enough to disrupt H12-induced dimerization. To potentiate the hydrophobic defects, we prepared two double mutants containing one substitution at each hydrophobic patch (L254A,F385A and W257A,M388A). Both double mutants showed reduced dimerization (Fig. 6). The SEC elution peaks of the L254A, F385A–H12 and W257A,M388A–H12 complexes were noticeably wider than for WT OPG–H12, indicating that double mutant OPG^{SH} was not able to dimerize as efficiently as WT OPG^{SH}. This result suggests that the same hydrophobic interface is required for HS-induced OPG dimerization.

Hydrophobic mutants show reduced binding to osteoblast HS

Although the identified hydrophobic residues cannot directly contribute to HS binding, which is typically mediated by ionic interactions and H-bonds (30), we reasoned that they might still promote OPG-HS interaction if dimerization and HS-binding is energetically coupled. In other words, just like HS-binding induces formation of $[OPG^{SH}]_2$ by promoting formation of the hydrophobic dimerization interface, formation of a stable dimerization interface might also favor HS-binding. To test this, we performed a flow cytometry-based OPG binding assay to evaluate whether the binding of OPG^{SH} to HS at the surface of MC3T3 cells is affected by hydrophobic mutations. As shown in Fig. 7, compared with WT OPG^{SH}, the binding of L254A,F385A and W257A,M388A OPG^{SH} to HS is reduced by about 67 and 53%, respectively. This result suggests that the hydrophobic interactions indeed promote OPG-HS interactions, likely by way of stabilizing the dimer interface. The occurrence of such mutually cooperative contacts has previously been noted for other proteins (31).

Hydrophobic residues are required for optimal activity of OPG toward RANKL

We have previously reported that HS on the surface of osteoblasts facilitates immobilization of OPG and consequently promotes OPG-RANKL interaction to inhibit osteoclastogenesis (5). Because we found now that the hydrophobic mutants show reduced binding to HS on osteoblast surface, we anticipate that these mutants might display impaired inhibition to osteoclastogenesis in bone marrow macrophage-osteoblast co-culture. In this system, primary osteoblasts are stimulated with vitamin D_3 and dexamethasone to induce expression of macrophage colony-stimulating factor and membrane-bound RANKL, which drives differentiation of co-cultured bone marrow macrophages into osteoclasts (2). Adding recombinant OPG into the system should dose-dependently inhibit RANKL and thus the extent of osteoclast differentiation (5, 32). As expected, L254A,F385A and W257A,M388A OPG^{SH} both showed reduced potency in inhibiting osteoclastogenesis compared with WT OPG^{SH}. When used at 1 μg/ml, WT OPG^{SH} was able to inhibit 88% of osteoclastogenesis as measured by TRAP activity, whereas L254A,F385A and W257A,M388A OPG^{SH} were only able to inhibit 38 and 44% of osteoclastogenesis (Fig. 8*A*). The difference is even more apparent when the osteoclasts were visualized by TRAP staining. Cells treated with 1 μg/ml of WT OPG^{SH} showed an absence of TRAP-positive cells with more than 10 cell nuclei, whereas abundant large to giant osteoclasts were present in samples treated with L254A,F385A and W257A,M388A OPG^{SH} (Fig. 8, *B–E*). This result provides direct evidence that an intact hydrophobic dimerization interface is required for the optimum inhibitory activity of OPG^{SH}.

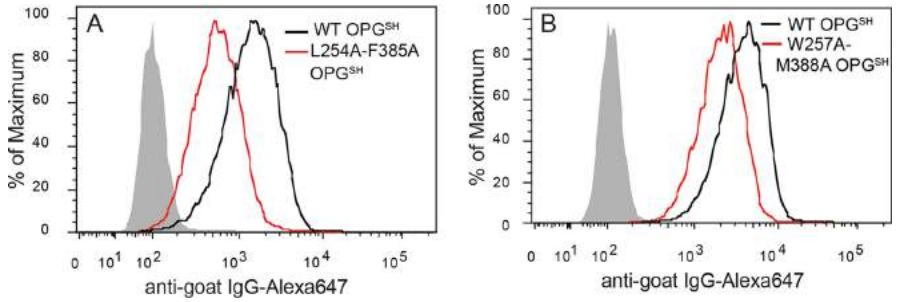

Figure 7. L254A,F385A and W257A,M388A OPG^{SH} show reduced binding to osteoblast HS. Binding of WT, L254A,F385A and W257A,M388A OPG^{SH} (1 μg/ml) to MC3T3 cells was determined by a FACS-based binding assay. The bound mOPG were detected by staining with a goat anti-mOPG antibody, followed by anti-goat IgG-Alexa 647. The *shaded histogram* is from cells stained only with antibodies.

To make sure that the intrinsic RANKL binding capacity and the structural integrity of the hydrophobic mutants are unaltered, we tested the inhibitory potency of the hydrophobic mutants toward RANKL in a monoculture assay using only bone marrow macrophages. Different from the co-culture system described above, no osteoblasts were present and the osteoclastogenesis was induced by exogenously added soluble RANKL (50 ng/ml). Therefore, the monoculture system allowed us to directly measure the inhibitory potency of OPG toward RANKL in solution without taking into account the role of osteoblast HS-OPG interaction. As expected, in this system, both hydrophobic double mutants showed identical inhibitory potency to the WT OPG at 1 μg/ml (Fig. 8*F*), which suggests that the hydrophobic mutants had no defect in inhibiting soluble RANKL, a strong indicator of their structural integrity. We further analyzed the binding kinetics of the hydrophobic mutants to immobilized RANKL by SPR (Table S1) and found that both hydrophobic mutants showed similar kinetic parameters to WT OPG, again suggesting that their structural integrity is minimally affected.

Discussion

Why OPG exists in both monomeric (OPG^{SH}) and as a covalently linked dimer (OPG$_2^{SS}$) and whether there is a functional difference between the two forms remains an open question. Our recent discovery that HS can induce OPG^{SH} to form a noncovalent dimer ([OPG^{SH}]$_2$) added a new dimension to this long-standing puzzle (5). What is unique about HS-induced [OPG^{SH}]$_2$ is that dimerization does not depend on the intermolecular (Cys-400–Cys-400′) disulfide bond. Yet, the structure of the [OPG^{SH}]$_2$–HS complex and the OPG$_2^{SS}$–HS complex is essentially the same as examined by small-angle X-ray scattering (5). The observation suggests two things. First, because the intermolecular disulfide bond is dispensable for forming [OPG^{SH}]$_2$, other intermolecular dimerization contact points must exist. Second, this dimerization interface must be insufficient to stabilize the dimer by itself, such that either intermolecular disulfide bond formation or HS-binding is required to stabilize the dimer. Thus, identification of this dimerization interface should provide significant insight into the OPG dimerization mechanism and its implications for the activity of OPG.

Despite extensive structural studies, our understanding of the working mechanics of OPG at the intact protein level remains rudimentary due to a lack of structural insight on the C-terminal half of the molecule. Recently, we and others have shown that osteoblast HS plays an essential role in immobilizing OPG on the cell surface and is required for OPG to inhibit RANKL properly by binding to the DD2 and tail domains (5, 32). Furthermore, we have obtained strong evidence that HS-binding converts OPG to a more compact and less flexible conformation, and that HS–OPG–RANKL form a stable ternary complex. These latest discoveries suggest that the C-terminal domains represent an allosteric hub of OPG and that the conformational changes initiated at the C-terminal domains could propagate into the N-terminal domains and impact on RANKL binding.

To gain more structural insight of OPG dimerization and understand the structural relationship between the N-terminal and C-terminal domains of OPG, we performed HDX-MS analysis of full-length OPG in various conditions in solution. Although HDX-MS has emerged as a valuable method to probe protein structure, to our knowledge it has not been leveraged to study protein–HS interactions (9). Our HDX-MS analysis of OPG has been proven to be fruitful in several regards. First, HDX-MS precisely pinpointed the HS-binding site of OPG, consistent with previous site-directed mutangenesis work (5). In fact, the protection from HDX offered by HS-binding represents the strongest effect that we see in our dataset (Fig. S6). Given that the HS-binding sites display no consensus sequence (30), our result strongly suggests that HDX-MS can be exploited as a prime method to expedite the identification of HS-binding site in HS-binding proteins, especially in cases where other high-resolution structural data are not available. Second, HDX-MS revealed that different from all other CRD domains, CRD4 has a rigid structure, possibly by forming strong interdomain interactions with DD1 (Fig. 9). Aided by the crystal structure of the RANKL–OPG(CRD1–4) complex, we identified a hydrophobic patch at the C-terminal tip of the CRD4, which was greatly protected from HDX in both OPG^{SH} and OPG$_2^{SS}$ (Fig. 4). One explanation for the HDX protection of this region is the formation of stable hydrophobic interactions with other regions of OPG. Based on the location of the patch, we predict that it likely binds to the beginning portion of DD1, which contains a large number of conserved hydrophobic residues. The presence of two conserved cysteines in the short linker region and DD1 further boosts our confidence in this

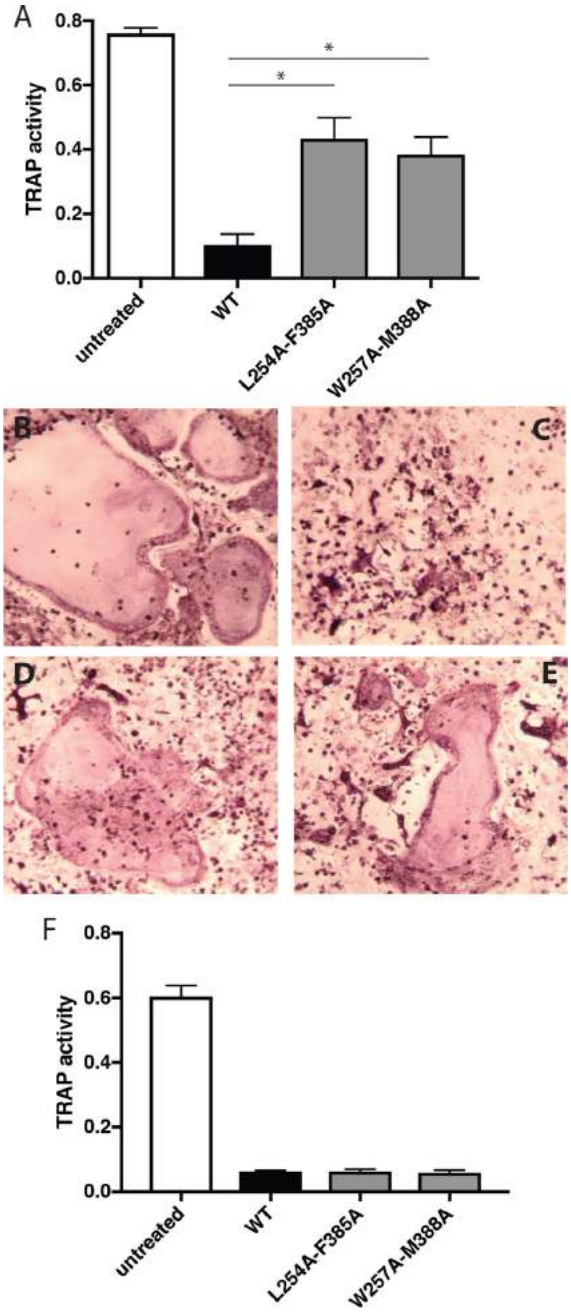

Figure 8. L254A,F385A and W257A,M388A OPG^{SH} show reduced inhibition of osteoclastogenesis. *A,* TRAP activity assay of the whole cell lysate after 6 days of co-culture of osteoblasts and bone marrow macrophage. Co-cultures were either untreated or treated with WT, L254A,F385A and W257A,M388A OPG^{SH} at 1 μg/ml ($n = 3$). *Error bars* represent S.D. * represents $p < 0.01$. Data are representative of three separate assays. *B–E,* representative images of differently treated OB-BMM co-cultures stained with a TRAP staining kit. *Panel B* is untreated control, *C* is treated with WT OPG^{SH}, *D* and *E* are treated with L254A,F385A and W257A,M388A OPG^{SH}, respectively. *F,* inhibition of osteoclastogenesis in bone marrow macrophage mono-culture by WT OPG or double mutant OPG at 1 μg/ml ($n = 3$). *Error bars* represent S.D. Osteoclastogenesis in this assay is induced by recombinant soluble RANKL (50 ng/ml) and macrophage-colony stimulating factor (20 ng/ml).

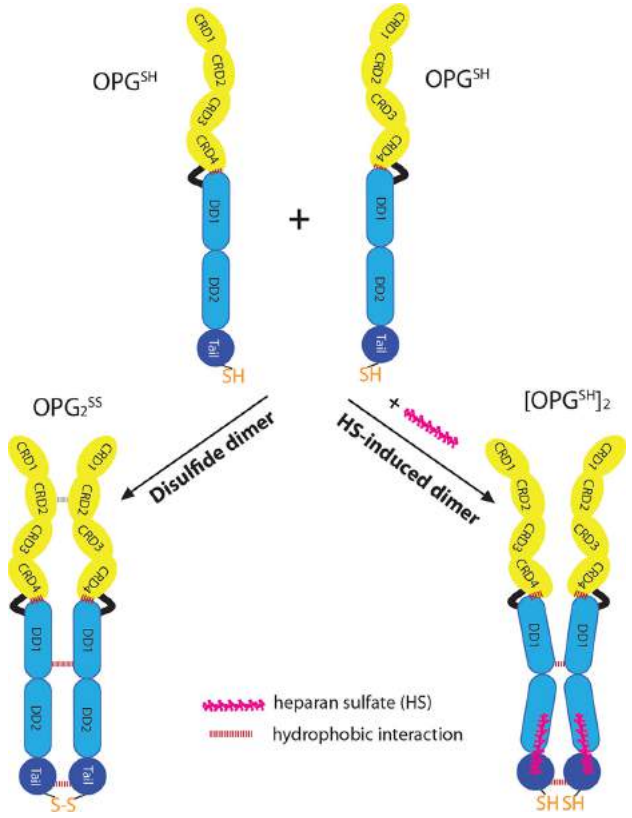

Figure 9. Schematic model of OPG dimerization mechanisms. Monomeric OPG (OPG^{SH}) can form a disulfide-linked covalent dimer (OPG$_2^{SS}$) and a HS-induced noncovalent dimer ([OPG^{SH}]2). OPG$_2^{SS}$ forms naturally in the cell, and its structure involves intermolecular hydrophobic interactions located in the DD1 and tail domains. The HS-induced [OPG^{SH}]2 formation involves both electrostatic interactions between HS and the DD2/tail domains, and intermolecular hydrophobic interactions located in the DD1 and tail domains. CRD2 domain displays intermolecular interactions in OPG$_2^{SS}$ but not in [OPG^{SH}]2. The nature of this particular interaction is unknown. HS-binding also induces significant conformational changes in OPG. The interaction between OPG and HS has a stoichiometry of 1:1.

prediction. Obviously, validation of our model would require solving the atomic structure of an OPG construct that includes both CRD4 and DD1, which we are currently pursuing. Finally, our HDX-MS data provided critical information that led to the identification of the dimerization interface of OPG. Identifying the location of potential protein interfaces is difficult without molecular structures but this study demonstrates the power of HDX-MS in aiding this task.

In our data set we found a number of peptides located in the C-terminal domains that were more protected in OPG–HS complex compared with free OPG. These peptides fall into two categories. One class of peptides cover part of the known HS-binding site of OPG, and HS-binding alone would explain their reduced HDX levels. The other class of peptides are, however, not part of the HS-binding site, yet HS-binding somehow led to their greatly reduced deuteration. We reasoned that the latter class of peptide might include residues that directly participate in dimerization, because the dimerization interface might only be stable enough (therefore display protection from HDX) when OPG is complexed with HS. The common feature of the

four peptides of interest (254–266, 304–332, 381–391, and 382–397) is that they all contain a high density of conserved hydrophobic residues, as well as basic resides. The potential involvement of the basic residues in dimerization through salt bridges can be ruled out because all 10 conserved basic residues within these peptides have been mutated previously and none of them showed much effect on dimerization (5). We then focused on the conserved hydrophobic residues because it is known that solvent-exposed hydrophobic residues are a major driver in protein oligomerization (28). Indeed, 8 of 11 hydrophobic residues that we tested had a greatly increased monomer/dimer ratio, with 4 of them displaying an absence of dimer. This dramatic effect on the monomer/dimer ratio by mutating just a single hydrophobic residue suggests there is a high likelihood that these residues are directly involved in dimerization. Of note, whereas peptide 304–332 was protected from HDX in the HS-bound OPG, it does not appear to directly participate in dimerization based on our mutagenesis study. One possibility that might lead to its protection is that this region is involved in the dramatic conformational change experienced by OPG upon HS-binding (5).

Interestingly, the hydrophobic residues that might participate in dimerization come from DD1 and the tail domain (Fig. 9). This is unexpected because these two domains do not directly connect to each other in sequence and are gapped by DD2. We envision two possible dimerization mechanisms. The first one is that two small dimerization interfaces might exist, one centered around residue 254–258 and another around residue 384–389, and they work independently by forming hydrophobic interactions with the corresponding regions on the other protomer (Fig. 9). The other possibility is that they work together and combine to form a large single dimerization interface. This would require that DD2 orient in such a way that brings the first death domain and the tail domain in close proximity. Either way, HS-binding is an essential factor to stabilize the otherwise weak hydrophobic intermolecular interactions. Based on the fact the hydrophobic mutants show greatly reduced occurrence of OPG_2^{SS}, we believe that our newly identified hydrophobic interface facilitates intermolecular disulfide bond formation, likely by providing a transient stabilization force during the process (Fig. 9).

Our study provided yet another example of hydrophobic interaction and HS-binding work synergistically to promote protein dimerization (Fig. 9). Previously, we have shown that in order for RAGE (receptor for advance glycation end product) to oligomerize, both a small hydrophobic dimerization interface and HS binding are required (33). Similar to the results of the current work, HS-binding mutants of RAGE had impaired oligomerization and the hydrophobic mutants of RAGE had reduced HS-binding affinity. Another example is amyloid precursor-like protein 1 (APLP-1), whose dimerization is promoted by heparin (34). Again, it was found that mutation of conserved hydrophobic residues at the dimerization interface had a negative effect on heparin binding, and most HS-binding mutants of APLP-1 showed impaired dimerization. Together, these findings suggest that energetically coupled hydrophobic intermolecular interaction and HS-binding may be a common mechanism for HS-induced oligomerization.

In conclusion, our study has provided new evidence that HS-binding is tightly knitted into OPG biology by regulating OPG dimerization. It can be expected that our discoveries will lead to a more comprehensive picture of the regulatory mechanism of OPG in bone remodeling and stimulate novel ways of manipulating the pathway.

Experimental procedures

Expression and purification of full-length mouse OPG

The expression and purification of full-length mouse OPG (mOPG) was performed using the method previously reported (5). The complete ORF of mOPG (GE Dharmacon) was cloned into pUNO1 (Invivogen) using NcoI and NheI sites. Transfection was performed using FectoPRO transfection reagent (Polyplus transfection). Recombinant mOPG was produced in 293-freestyle cells (ThermoFisher Scientific). Purification of mOPG from culture supernatant was carried out using a HiTrap heparin-Sepharose column (GE Healthcare) at pH 7.1 (HEPES buffer), followed by gel permeation chromatography on a Superdex 200 column in 20 mM Tris, 150 mM NaCl, pH 7.4 (GE Healthcare). After purification, mOPG was 99% pure as judged by silver staining, and mOPG monomers were fully separated from dimers. Throughout the study, we used the K241A,R242A,R243Q (AAQ) mutant interchangeably with WT mOPG because of its higher expression level. The AAQ mutant performed equivalently as WT mOPG in HS-binding, dimerization and osteoclastogenesis assays.

Surface plasma resonance

Porcine intestinal HS (14 kDa, Celsus Laboratories, Cincinnati, OH) was biotinylated by sulfo-NHS long-chain biotin (ThermoFisher) with free amino groups of unsubstituted glucosamine residues in the polysaccharide chain following a published procedure (35). The biotinylated HS was immobilized to a streptavidin chip based on the manufacturer's protocol. In brief, 20 μl of solution of the HS-biotin conjugate (0.1 mg/ml) in HBS-EP running buffer (0.01 M HEPES, pH 7.4, 0.15 M NaCl, 3 mM EDTA, 0.005% (v/v) Surfactant P20) was injected over flow cell 2 of the streptavidin chip at a flow rate of 10 μl/min. The successful immobilization of HS was confirmed by the observation of a 100–200 resonance unit increase in the sensor chip. The control flow cell 1 was prepared by a 1-min injection with saturated biotin. Different dilutions of protein samples (concentrations from 1.25 to 160 nM) in HBS-EP buffer were injected at a flow rate of 30 μl/min. At the end of the sample injection, the same buffer was flowed over the sensor surface to facilitate dissociation. After a 3-min dissociation time, the sensor surface was regenerated by injecting with 30 μl of 0.25% SDS to get fully regenerated surface. The sensorgrams were fit with 1:1 Langmuir binding model from BIAevaluate 4.0.1.

For measuring RANKL-OPG interactions, the recombinant RANKL extracellular domain was immobilized on CM5 chips according to standard amine coupling protocol (GE Healthcare, Uppsala, Sweden). Different dilutions of OPG or mutants (6.25 to 200 nM) were injected at a flow rate of 30 μl/min with HBS-EP buffer as a running buffer followed by a 3-min dissociation time.

Isolation and purification of OPG from bone marrow plasma and cell surface

Tibias and femurs from one WT BL/6 mouse were collected to isolate OPG. Collection of these tissues were approved by the Institutional Animal Care and Use Committee of the University at Buffalo. Bone marrow cavities were flushed with 0.6 ml of PBS and the cells were centrifuged to collect the supernatant, which contained soluble OPG. The bone marrow cell pellets were then washed with PBS and incubated with 0.6 ml of 1.5 M NaCl for 5 min at room temperature. The high salt wash, which contains the cell surface-associated OPG was collected after cells were centrifuged. The high salt wash was then diluted by 25 mM HEPES, pH 7.1, to a final salt concentration of 150 mM. Purifications of both PBS wash and diluted high salt wash were carried out with the same method for recombinant mOPG purification using a HiTrap heparin-Sepharose column, eluent was collected in 1-ml fractions, and the quantity of OPG determined by a sandwich ELISA.

OPG ELISA

OPG was measured by sandwich ELISA. Briefly, a 96-well plate was coated by goat anti-mOPG antibody (R&D Systems, AF574) and blocked by 1% BSA. Recombinant mOPG with concentrations at 25 pg to 1.5 ng/ml was used to make the standard curve, heparin column fractions were added into wells and incubated for 2 h followed by incubation with biotinylated rabbit anti-mOPG antibody (made in house) for 1 h and streptavidin-horseradish peroxidase for 30 min. 50 μl of horseradish peroxidase substrate solution was added for developing, and the reaction was stopped by adding 50 μl of 1 M H_2SO_4, the absorbance at 450 nm was measured by a plate reader. Concentrations of OPG in each fraction were calculated with Straightforward ELISA software online.

HDX samples

HDX samples were prepared in 25 mM HEPES, 50 mM NaCl, and 85% D_2O (HDX buffer) at pH_{read} 7.1 at room temperature, 22 ± 1 °C. All samples contained 8 μM OPG_2^{SS} or 16 μM OPG^{SH}. RANKL trimer was added at a concentration of 7.5 μM, and heparin-derived dodecasaccharide (H12) at 11.4 μM. On the basis of nanomolar literature K_d values (8, 36) for HS interactions with RANKL, OPG was ~99% saturated with its binding partners under HDX conditions. A stoichiometric excess of RANKL was chosen to suppress the presence of free OPG. This scenario precluded meaningful HDX measurements on RANKL because a significant fraction of RANKL chains remained unbound. The OPG response to ligand binding was probed by conducting HDX-MS on eight types of samples: 1) OPG^{SH} without binding partners, 2) OPG^{SH} + HS, OPG^{SH} + HS + RANKL, 4) OPG^{SH} + RANKL, 5) OPG_2^{SS} without binding partners, 6) OPG_2^{SS} + HS, 7) OPG_2^{SS} + HS + RANKL, and 8) OPG_2^{SS} + RANKL. 10-μl aliquots were removed from the HDX solutions at 10 s, 1 min, 10 min, 50 min, 100 min, and 200 min. In initial digestion experiments we found that the high number of disulfides in the OPG CRD1–CRD4 region caused poor sequence coverage, a problem that is commonly encountered with SS-containing proteins (19–22). After extensive testing and optimization we settled on a disulfide reduction strategy involving TCEP (20, 37). Aliquots (10 μl) were mixed in a 1:1 volume ratio with ice-cold quenching buffer (8 M urea and 1 M TCEP·HCl) at a measured pH of 2.3. The samples were then flash frozen in liquid nitrogen and stored at −80 °C. Prior to analysis the samples were thawed to 0 °C, and the liquid samples were kept on ice for 5 min for TCEP-mediated disulfide reduction. The samples were then diluted with 3 volumes of aqueous formic acid, pH 2.3, to lower the TCEP concentration for protecting the downstream pepsin column. The resulting 60-μl samples were analyzed as outlined below. The reduction/digestion workflow resulted in 60+ peptides for a sequence coverage of ~80%. The digestion patterns of OPG_2^{SS} and OPG^{SH} were slightly different. Although the use of TCEP significantly improved peptic digestion of the CRD regions, the number of peptides originating from this region was significantly lower than in the DD1/DD2/Tail regions (Figs. S1 and S2). Zero-time point samples (m_0) were produced by exposing pre-quenched OPG to D_2O labeling solution. Maximally exchanged controls (m_{100}) were generated by incubation of OPG in HDX solution at pH 2.4 for 24 h and 37 °C. In all other aspects, the m_0 and m_{100} samples were treated like the regular time points.

HDX-MS analysis

Quenched aliquots (60 μl) were injected into a nanoACQUITY UPLC with HDX technology (Waters, Milford, MA) for digestion, desalting, and peptide separation. Online digestions were performed on a POROS pepsin column (2.1 × 30 mm, Applied Biosystems, Carlsbad, CA) at 15 °C. The resulting peptides were trapped on a guard column (BEH C18 1.7 μm, 2.1 × 5 mm) and separated on a reversed phase column (BEH C18 1.7 μm, 1 × 100 mm) using a water/acetonitrile gradient in the presence of 0.1% formic acid at 40 μl min^{-1}. Peptide mass spectra was recorded on a Wates Synapt G2 instrument with source and desolvation temperatures of 80 and 250 °C, respectively. The cone voltage was set at 20 V, and the electrospray voltage was 3 kV. The identity of each peptide was confirmed by MS^E and PLGS 2.4.3 (Waters) in initial control experiments conducted without D_2O. HDX kinetic profiles were analyzed by DynamX 3.0 (Waters) and plotted as centroid mass *versus* D_2O exposure time. Deuteration levels are reported as *HDX Percentage* $= (m_t - m_0)/(m_{100} - m_0)$. All experiments were performed in triplicate. Error bars represent standard deviations.

Site-directed mutagenesis

Mouse OPG mutants were prepared using published methods (5). Mutations were confirmed by sequencing, and recombinant protein was expressed and purified as described for WT mOPG.

Analytical size-exclusion chromatography

For analyses of mOPG and heparan sulfate dodecasaccharide (H12) complex, purified WT OPG monomer, or mutant OPG monomer (30 μg) were incubated with H12 (2 μg) in 20 mM Tris, 150 mM NaCl, pH 7.4, at room temperature for 2 h. All complexes were resolved on an Enrich SEC 650 column (10/300 mm, Bio-Rad) using 20 mM Tris, 150 mM NaCl, pH 7.4, at 4 °C.

Flow cytometry-based binding assay

MC3T3-E1 cells were lifted from the culture dish using Accutase (Biolegend) and incubated with WT monomer or mutant mOPG monomer (1 μg/ml) in 100 μl of PBS, 0.1% BSA for 1 h at 4 °C. Bound mOPG was stained with goat anti-mouse OPG (400 ng/ml, AF459, R&D Systems) for 1 h at 4 °C, followed by anti-goat IgG-Alexa 647 (1:1000, ThermoFisher Scientific) for 30 min and analyzed by flow cytometry. The apparent binding affinity between OPG and cell-surface HS was calculated by using the geometric means of Alexa 647 fluorescence intensity as the binding signal.

Osteoclastogenesis assay

Co-culture osteoclastogenesis assay—Primary osteoblasts were isolated from calvaria of 5–8–day-old WT mice following an established protocol (38). Osteoblasts (5×10^3 cells/well) were seeded in a 96-well plate the day before starting the co-culture. Freshly isolated bone marrow cells (from one WT mouse) were suspended in 10 ml of α-minimal essential medium containing 10% FBS and 1 penicillin/streptomycin, 10^{-7} M dexamethasone, and 10^{-8} M 1α- and 25-dihydroxyvitamin D_3. 100 μl of bone marrow cells were added into each well. In selected wells, 1 μg/ml of WT or double mutants OPG monomer (L254A,F385A and W257A,M388A) were added. The unattached cells were removed after 24 h in culture and the medium was replaced. The medium was replaced every 2 days thereafter until the appearance of giant osteoclasts. To visualize osteoclasts, the cells were fixed and stained for TRAP activity using an Leukocyte Acid Phosphatase kit (Sigma). For quantitative measurement of TRAP activity, cells were lysed with 50 μl of lysis buffer (50 mM Tris, pH 7.5, 150 mM NaCl, 1% Nonidet P-40) for 30 min at 4 °C. 10 μl of lysate were then mixed with 50 μl of TRAP assay buffer containing 0.5 M sodium acetate, 10 mM tartrate, and 10 mM *p*-nitrophenyl phosphate substrate and incubated at 37 °C for 15 min. The reaction was stopped by adding 50 μl of 0.5 N NaOH, and the absorbance at 405 nm was measured by a plate reader.

Mono-culture osteoclastogenesis assay—20 ng/ml of macrophage-colony stimulating factor (Peprotech) and 50 ng/ml of soluble RANKL (prepared in house with endotoxin level <0.1 EU/μg of protein) were used to induce osteoclastogenesis of nonadherent murine bone marrow cells. WT or double mutant OPG were added at 1 μg/ml. After appearance of giant osteoclasts, cells were lysed and assayed for TRAP activity as described above.

Author contributions—Y. X., M. L., R. L., F. Z., A. M., J. C., L. K., and D. X. data curation; Y. X., M. L., R. L., F. Z., A. M., J. C., L. K., and D. X. formal analysis; Y. X., M. L., F. Z., L. K., and D. X. validation; Y. X., M. L., R. L., F. Z., L. K., and D. X. investigation; Y. X., M. L., F. Z., L. K., and D. X. visualization; Y. X., M. L., R. L., F. Z., L. K., and D. X. methodology; Y. X., M. L., L. K., and D. X. writing-original draft; F. Z., L. K., and D. X. conceptualization; R. J. L., L. K., and D. X. resources; R. J. L., L. K., and D. X. software; R. J. L., L. K., and D. X. funding acquisition; R. J. L., L. K., and D. X. writing-review and editing; L. K. and D. X. supervision; L. K. and D. X. project administration.

Acknowledgment—We thank Dr. Lars Pedersen for reviewing the manuscript.

References

1. Simonet, W. S., Lacey, D. L., Dunstan, C. R., Kelley, M., Chang, M. S., Lüthy, R., Nguyen, H. Q., Wooden, S., Bennett, L., Boone, T., Shimamoto, G., DeRose, M., Elliott, R., Colombero, A., Tan, H. L., Trail, G., Sullivan, J., Davy, E., *et al.* (1997) Osteoprotegerin: a novel secreted protein involved in the regulation of bone density. *Cell* **89,** 309–319 CrossRef Medline
2. Udagawa, N., Takahashi, N., Yasuda, H., Mizuno, A., Itoh, K., Ueno, Y., Shinki, T., Gillespie, M. T., Martin, T. J., Higashio, K., and Suda, T. (2000) Osteoprotegerin produced by osteoblasts is an important regulator in osteoclast development and function. *Endocrinology* **141,** 3478–3484 CrossRef Medline
3. Nelson, C. A., Warren, J. T., Wang, M. W., Teitelbaum, S. L., and Fremont, D. H. (2012) RANKL employs distinct binding modes to engage RANK and the osteoprotegerin decoy receptor. *Structure* **20,** 1971–1982 CrossRef Medline
4. Yamaguchi, K., Kinosaki, M., Goto, M., Kobayashi, F., Tsuda, E., Morinaga, T., and Higashio, K. (1998) Characterization of structural domains of human osteoclastogenesis inhibitory factor. *J. Biol. Chem.* **273,** 5117–5123 CrossRef Medline
5. Li, M., Yang, S., and Xu, D. (2016) Heparan sulfate regulates the structure and function of osteoprotegerin in osteoclastogenesis. *J. Biol. Chem.* **291,** 24160–24171 CrossRef Medline
6. Tsuda, E., Goto, M., Mochizuki, S., Yano, K., Kobayashi, F., Morinaga, T., and Higashio, K. (1997) Isolation of a novel cytokine from human fibroblasts that specifically inhibits osteoclastogenesis. *Biochem. Biophys. Res. Commun.* **234,** 137–142 CrossRef Medline
7. Luan, X., Lu, Q., Jiang, Y., Zhang, S., Wang, Q., Yuan, H., Zhao, W., Wang, J., and Wang, X. (2012) Crystal structure of human RANKL complexed with its decoy receptor osteoprotegerin. *J. Immunol.* **189,** 245–252 CrossRef
8. Schneeweis, L. A., Willard, D., and Milla, M. E. (2005) Functional dissection of osteoprotegerin and its interaction with receptor activator of NF-κB ligand. *J. Biol. Chem.* **280,** 41155–41164 CrossRef Medline
9. Konermann, L., Pan, J., and Liu, Y. H. (2011) Hydrogen exchange mass spectrometry for studying protein structure and dynamics. *Chem. Soc. Rev.* **40,** 1224–1234 CrossRef Medline
10. Xiao, H., Hoerner, J. K., Eyles, S. J., Dobo, A., Voigtman, E., Mel'cuk, A. I., and Kaltashov, I. A. (2005) Mapping protein energy landscapes with amide hydrogen exchange and mass spectrometry: I. a generalized model for a two-state protein and comparison with experiment. *Protein Sci.* **14,** 543–557 CrossRef Medline
11. Wales, T. E., and Engen, J. R. (2006) Hydrogen exchange mass spectrometry for the analysis of protein dynamics. *Mass Spectrom. Rev.* **25,** 158–170 CrossRef Medline
12. Rand, K. D., Zehl, M., and Jørgensen, T. J. (2014) Measuring the hydrogen/deuterium exchange of proteins at high spatial resolution by mass spectrometry: overcoming gas-phase hydrogen/deuterium scrambling. *Acc. Chem. Res.* **47,** 3018–3027 CrossRef Medline
13. Percy, A. J., Rey, M., Burns, K. M., and Schriemer, D. C. (2012) Probing protein interactions with hydrogen/deuterium exchange and mass spectrometry: a review. *Anal. Chim. Acta* **721,** 7–21 CrossRef Medline
14. Marciano, D. P., Dharmarajan, V., and Griffin, P. R. (2014) HDX-MS guided drug discovery: small molecules and biopharmaceuticals. *Curr. Opin. Struct. Biol.* **28,** 105–111 CrossRef Medline
15. Maaty, W. S., and Weis, D. D. (2016) Label-free, in-solution screening of peptide libraries for binding to protein targets using hydrogen exchange mass spectrometry. *J. Am. Chem. Soc.* **138,** 1335–1343 CrossRef Medline
16. Skinner, J. J., Lim, W. K., Bédard, S., Black, B. E., and Englander, S. W. (2012) Protein dynamics viewed by hydrogen exchange. *Protein Sci.* **21,** 996–1005 CrossRef Medline
17. Shaw, B. F., Arthanari, H., Narovlyansky, M., Durazo, A., Frueh, D. P., Pollastri, M. P., Lee, A., Bilgicer, B., Gygi, S. P., Wagner, G., and Whitesides, G. M. (2010) Neutralizing positive charges at the surface of a protein

lowers its rate of amide hydrogen exchange without altering its structure or increasing its thermostability. *J. Am. Chem. Soc.* **132,** 17411–17425 CrossRef Medline
18. Anderson, J. S., Hernández, G., and Lemaster, D. M. (2008) A billion-fold range in acidity for the solvent-exposed amides of *Pyrococcus furiosus* rubredoxin. *Biochemistry* **47,** 6178–6188 CrossRef Medline
19. Zhang, J., Ogorzalek Loo, R. R., and Loo, J. A. (2015) Increasing fragmentation of disulfide-bonded proteins for top-down mass spectrometry by supercharging. *Int. J. Mass Spectrom.* **377,** 546–556 CrossRef Medline
20. Zhang, H. M., McLoughlin, S. M., Frausto, S. D., Tang, H., Emmett, M. R., and Marshall, A. G. (2010) Simultaneous reduction and digestion of proteins with disulfide bonds for hydrogen/deuterium exchange monitored by mass spectrometry. *Anal. Chem.* **82,** 1450–1454 CrossRef Medline
21. Trabjerg, E., Jakobsen, R. U., Mysling, S., Christensen, S., Jørgensen, T. J., and Rand, K. D. (2015) Conformational analysis of large and highly disulfide-stabilized proteins by integrating online electrochemical reduction into an optimized H/D exchange mass spectrometry workflow. *Anal. Chem.* **87,** 8880–8888 CrossRef Medline
22. Wongkongkathep, P., Li, H., Zhang, X., Loo, R. R., Julian, R. R., and Loo, J. A. (2015) Enhancing protein disulfide bond cleavage by UV excitation and electron capture dissociation for top-down mass spectrometry. *Int. J. Mass Spectrom* **390,** 137–145 CrossRef Medline
23. Pantazatos, D., Kim, J. S., Klock, H. E., Stevens, R. C., Wilson, I. A., Lesley, S. A., and Woods, V. L., Jr. (2004) Rapid refinement of crystallographic protein construct definition employing enhanced hydrogen/deuterium exchange MS. *Proc. Natl. Acad. Sci. U.S.A.* **101,** 751–756 CrossRef Medline
24. Shukla, A. K., Westfield, G. H., Xiao, K., Reis, R. I., Huang, L. Y., Tripathi-Shukla, P., Qian, J., Li, S., Blanc, A., Oleskie, A. N., Dosey, A. M., Su, M., Liang, C. R., Gu, L. L., Shan, J. M., *et al.* (2014) Visualization of arrestin recruitment by a G-protein-coupled receptor. *Nature* **512,** 218–222 CrossRef Medline
25. Burke, J. E., Babakhani, A., Gorfe, A. A., Kokotos, G., Li, S., Woods, V. L., Jr., McCammon, J. A., and Dennis, E. A. (2009) Location of inhibitors bound to group IVA phospholipase A2 determined by molecular dynamics and deuterium exchange mass spectrometry. *J. Am. Chem. Soc.* **131,** 8083–8091 CrossRef Medline
26. Sowole, M. A., Alexopoulos, J. A., Cheng, Y. Q., Ortega, J., and Konermann, L. (2013) Activation of ClpP protease by ADEP antibiotics: insights from hydrogen exchange mass spectrometry. *J. Mol. Biol.* **425,** 4508–4519 CrossRef Medline
27. Bobst, C. E., Zhang, M., and Kaltashov, I. A. (2009) Existence of a noncanonical state of iron-bound transferrin at endosomal pH revealed by hydrogen exchange and mass spectrometry. *J. Mol. Biol.* **388,** 954–967 CrossRef Medline
28. Goodsell, D. S., and Olson, A. J. (2000) Structural symmetry and protein function. *Annu. Rev. Biophys. Biomol. Struct.* **29,** 105–153 CrossRef Medline
29. Kelley, L. A., Mezulis, S., Yates, C. M., Wass, M. N., and Sternberg, M. J. (2015) The Phyre2 web portal for protein modeling, prediction and analysis. *Nat. Protoc.* **10,** 845–858 CrossRef Medline
30. Xu, D., and Esko, J. D. (2014) Demystifying heparan sulfate-protein interactions. *Annu. Rev. Biochem.* **83,** 129–157 CrossRef Medline
31. Creighton, T. E. (1993) *Proteins: structures and molecular properties*, W. H. Freeman & Co., New York
32. Nozawa, S., Inubushi, T., Irie, F., Takigami, I., Matsumoto, K., Shimizu, K., Akiyama, H., and Yamaguchi, Y. (2018) Osteoblastic heparan sulfate regulates osteoprotegerin function and bone mass. *JCI Insight* **3,** pii 89624 Medline
33. Xu, D., Young, J. H., Krahn, J. M., Song, D., Corbett, K. D., Chazin, W. J., Pedersen, L. C., and Esko, J. D. (2013) Stable RAGE-heparan sulfate complexes are essential for signal transduction. *ACS Chem. Biol.* **8,** 1611–1620 CrossRef Medline
34. Xue, Y., Lee, S., and Ha, Y. (2011) Crystal structure of amyloid precursor-like protein 1 and heparin complex suggests a dual role of heparin in E2 dimerization. *Proc. Natl. Acad. Sci. U.S.A.* **108,** 16229–16234 CrossRef Medline
35. Hernaiz, M., Liu, J., Rosenberg, R. D., and Linhardt, R. J. (2000) Enzymatic modification of heparan sulfate on a biochip promotes its interaction with antithrombin III. *Biochem. Biophys. Res. Commun.* **276,** 292–297 CrossRef Medline
36. Baud'huin, M., Ruiz-Velasco, C., Jego, G., Charrier, C., Gasiunas, N., Gallagher, J., Maillasson, M., Naggi, A., Padrines, M., Redini, F., Duplomb, L., and Heymann, D. (2011) Glycosaminoglycans inhibit the adherence and the spreading of osteoclasts and their precursors: role in osteoclastogenesis and bone resorption. *Eur. J. Cell Biol.* **90,** 49–57 CrossRef Medline
37. Zhao, D. S., Gregorich, Z. R., and Ge, Y. (2013) High throughput screening of disulfide-containing proteins in a complex mixture. *Proteomics* **13,** 3256–3260 CrossRef Medline
38. Taylor, S. E., Shah, M., and Orriss, I. R. (2014) Generation of rodent and human osteoblasts. *Bonekey Rep.* **3,** 585 Medline

Dimerization interface of osteoprotegerin revealed by hydrogen–deuterium exchange mass spectrometry

Yiming Xiao, Miaomiao Li, Rinzhi Larocque, Fuming Zhang, Anju Malhotra, Jianle Chen, Robert J. Linhardt, Lars Konermann and Ding Xu

J. Biol. Chem. 2018, 293:17523-17535.
doi: 10.1074/jbc.RA118.004489 originally published online September 25, 2018
